OPEN ACCESS

GAVIN PUBLISHERS

Biosensors and Bioelectronics Open Access

Research Article

Najjar YSH and Mashareh S. Biosens Bioelectron Open Acc: BBOA-139.

DOI: 10.29011/ 2577-2260.100039

Performance Improvement of Hydrogen Sensors in Support of Greening the Future of Energy

Yousef S. H. Najjar*, Samaher Mashareh

Department of Mechanical Engineering, Jordan University of Science and Technology, Irbid, Jordan

***Corresponding author:** Yousef S. H. Najjar, Department of Mechanical Engineering, Jordan University of Science and Technology, Irbid, Jordan. Tel: +962785793463; Fax: +96227100836; Email: y_najjar@hotmail.com

Citation: Najjar YSH, Mashareh S (2018) Performance Improvement of Hydrogen Sensors in Support of Greening the Future of Energy. Biosens Bioelectron Open Acc: BBOA-139. DOI: 10.29011/ 2577-2260.100039

Received Date: 28 June, 2018; **Accepted Date:** 06 August, 2018; **Published Date:** 13 August, 2018

Abstract

Hydrogen has the greatest probability to leak. So, hydrogen detection becomes more challenging than other gases for safety considerations. In this study, Electro-thermal simulation and transient analysis for hydrogen leakage semiconductor sensor were performed. The heater coil and the sensitive layer of the sensor are the main investigated parts. Finite Element Method (FEM) analysis used to compare the electro-thermal properties of two geometrical heater coils and different materials for sensitive layer. The temperature of the simulated sensors was analysed considering the natural convection and radiation, ambient temperature variation from 0-50°C, varying heater coil materials, varying dimensions, and varying sensitive layer materials. Optimization for the heater coil was performed by comparing the maximum surface temperature, power consumption, and the time response for both sensor designs by COMSOL 4.3. The simulated results confirmed that the nickel-chrome material for the heater needs minimum power consumption of 82% lower than Pt. But it has longer response time, which is 37 seconds (240% of Pt response time) at 1V power supply. Also, Comparing SnO2 and ZnO sensitive materials, SnO2 material has a response time lower than ZnO by 28% in helical based sensor and 31% in meander one. Finally, the helical based sensor needs power less than meander one by 40% to achieve the 350°C surface temperature. In other words, helical based sensor generates higher surface temperature by 36% from the meander one at the same power consumption (500mW power supply).

Introduction

Several gas sensors using n-type semiconductor oxide such as SnO_2 detects different kinds of reducing or oxidizing gases in the air from a change of its resistance. Since early proposed by Seiyama and Taguchi half a century ago [1], various sensors have been developed and commercialized for various purposes. Yet there are still many demands to gas sensors. For example, various novel sensors are on the list of urgent developments, especially micro - scale gas sensors using MEMS (micro electromechanical system) technique. Metal oxide semiconductor sensors have been used extensively to detect toxic and harmful gases [2,3]. The most representative sensing materials are SnO_2 [4,5] and ZnO [6,7], which are n-type semiconductor material. Also, other n-type semiconductors such as TiO_2 [8,9], WO_3 [10,11], In_2O_3 [12,13], and Fe_2O_3 [14,15] are widely being researched to find new functionalities as a resistive semiconductor sensor. In contrast, the resistive semiconductor sensors using p-type materials relatively have received little attention.

Recently, MOS gas sensors need to have fast response, low power consumption, and uniform temperature distribution through the sensing material. Also, they require good mechanical stability at high temperatures. These requirements, together with good thermal isolation from the surrounding components obtained by means of silicon micromachining technology [16]. In general, the conventionally MOX sensing device, usually the sensitive material is embedded in a porous sintered alumina structure and formed as a bead around a heater coil. The hydrogen can diffuse inside the sensitive material pores and interact with it, which lowering the surface potential, and hence the resistance of the sensitive layer [17]. While micro-machined MOX gas sensing devices have been extensively researched and reviewed. The micro-machined sensing devices consisted of an insulating membrane with electrodes at the top surface on which the MOX sensing material was deposited [18]. An integrated heater was fabricated at the lower side of the membrane. This micro-machined sensor design had lower power consumption comparing with that of conventional one. Also, micromachining enhanced other performance metrics, such as

dynamic range and Lower Detection Limit (LDL). Experimental assessments, as discussed in Ref. [19] observe that not all micro machined MOX sensing devices or elements show improved performance relative to conventional MOX sensing elements.

In semiconductor sensors the active area comprises a heater coil, sensor electrodes and the gas-sensitive layer in the centre of a thin membrane. This membrane provides thermal isolation between the heated coil and the sensitive layer [20,21]. For gas sensing purposes, the operating temperature of the sensitive layer should be from 300 - 500°C [22,23], so requiring high power (more than 800mW) consumed by the heating device. The best performance of the gas sensors requires uniform temperature distribution through the sensitive layer, and very low thermal inertia to allow the response of the sensors to be fast enough [24]. This is very important when working in thermal- pulsed operation mode [25,26] mainly to minimize the consumed power and enhance the sensor selectivity. In this study, using 3D Finite Element Method (FEM) tools, we investigate two heater coil geometrical designs, helical coil and meander heater coil. The meander one usually used in thin and thick film semiconductor sensors [27]. The heater coil in both designs is suspended on the nickel plated copper pins instead of using insulating membrane as in thin or thick film sensors, in order to achieve good mechanical stability and thermal isolation for the heater coil. In this study, three different materials and dimensions for both heater coils were simulated, and the power consumption for both heater coils were compared. The simulated materials are nickel-chrome alloy, platinum and low cost nickel alloy called Dilverp1 [28] (an alloy of Ni, Co, Fe). These materials are thermally and electrically stable at high temperature, and available widely for fabrication process; also they are highly conductive, so require a low power supply.

Furthermore, the effects of natural cooling factors resulted from convection and radiation were considered. As well as investigating the effects of changing the ambient temperature. Also, the electrically insulating layer of Alumina material (Al_2O_3) was implemented for both geometries. Finally, sensitive layer of two materials (SnO_2 and ZnO) were investigated by means of transient thermal analysis. And the simulation results for two sensor geometries were compared to achieve low power consumption, uniform thermal distribution, and fast response (to reach the maximum temperature) through the surface of the sensitive layer. Figure 1 observes schematic of the simulated helical based sensor.

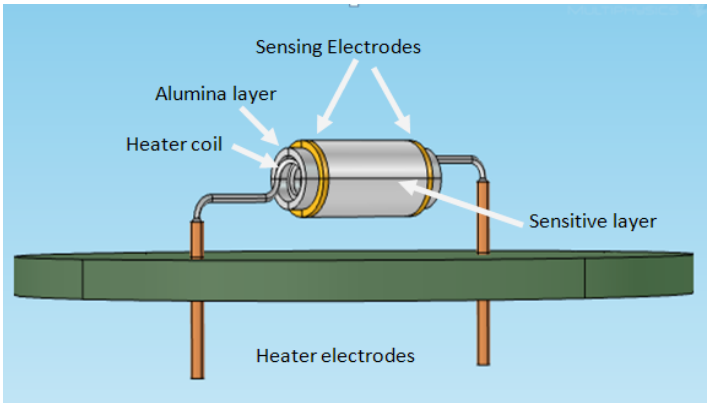

Figure 1: Schematic design of simulated MOS helical based sensor. Meander based sensor design has the same configuration but using meander heater coil instead of helical one.

The heat distribution simulated in 2D models is not so good because of the heat spreading, so quite high power consumption. This is enhanced by using a 3D model. This design has faster heating characteristics and uniform heating of the sensor surface. The main advantage of using software simulation is to make design optimization just by varying geometries, materials, and dimensions of your device before actual fabrication. Thus, saving time and cost needs for testing and fabrication procedures [29].

Geometry of Simulated Sensors

The simulated sensors are represented by two geometrical designs, using helical heater coil and meander heater coil. Schematics of helical and meander coil is shown in Figure 2. Each sensor consists of five components: a metallic pin made of Nickel (Ni) plated Copper (Cu) connecting the coil to other devices, a plastic board that represents the sensor base usually electrical insulator made of fiber reinforced epoxy (FR4), a heater coil, Al_2O_3 layer, and sensitive layer with it electrodes. Also, alumina and sensitive material layers were implemented for both coils. Alumina layer used to conduct the heat to the sensitive layer and support it mechanically. In this simulation the basic materials and dimensions used for the whole structure except the coil itself and the sensitive layer are the same in both simulated models. Also, the heat transfer between the helical coil and alumina layer is considered to be by conduction, because of micro-scale space, and several contact points between the coil and the layer (the layer is not separated from the coil).

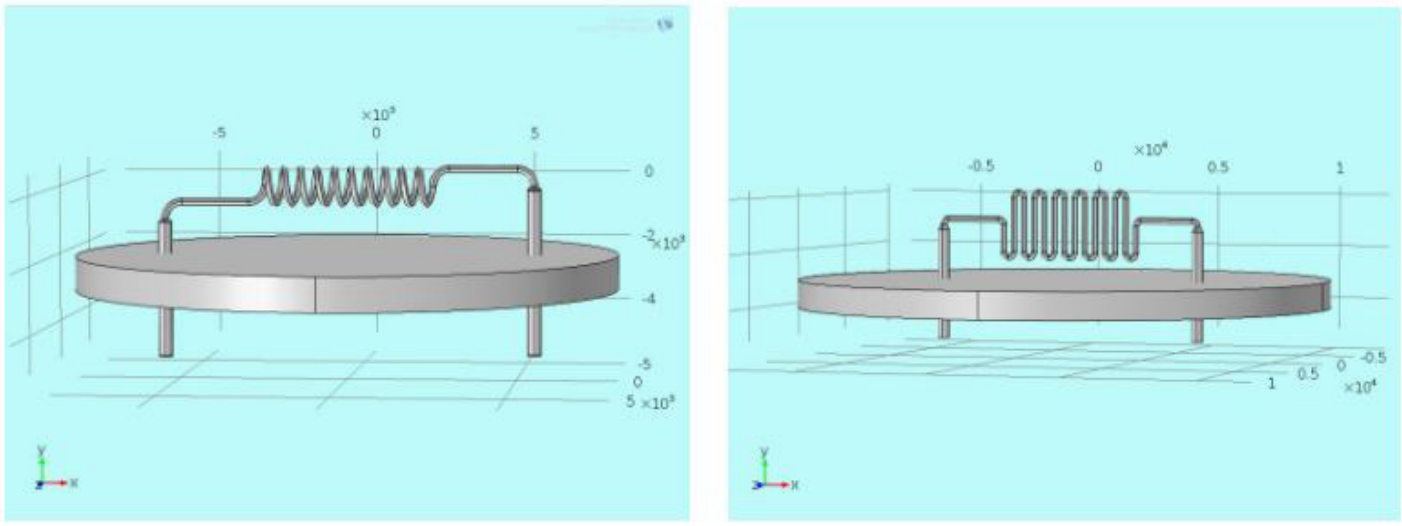

(a) (b)

Figure 2: Heater coil designs **(a)** helical heater coil **(b)** meander heater coil.

Numerical Model - Governing Equations, Boundary and Initial Conditions

As mentioned above, the heat generated in the heater coil by electrical current is a classical joule heating physical model. A given electrical current I_0 induces an electrical potential V_0 whose magnitude depends on the characteristics of the heater coil material. During joule heating, the temperature increases by the resistive heating from the electrical current. The electrical potential V_0 is the solution variable in the Conductive Direct Current (DC) application mode. The resistive heat Q generated in the model is proportional to the square of the magnitude of the electric current density J, which is proportional to the electric field, and equals the negative of the gradient of the potential V_0, so we have [28]:

$$Q \alpha |J^2| \quad (1)$$

$$Q = {}^{1}/_{\sigma} \cdot |J^2| = {}^{1}/_{\sigma} \cdot |\sigma E|^2 = \sigma |\Delta V_0|^2 \quad (2)$$

The coefficient of proportionality is the electric resistivity (ρ_R=1/σ, where σ is the electric conductivity) [106]. In a range of temperatures, the electrical conductivity σ is a function of temperature, According to the next formula:

$${}^{\sigma_0}/_{(1+\alpha_R(T-T_0)} \quad (3)$$

Where σ_0 is the conductivity at the reference temperature T_0, and α_R is the temperature coefficient of resistivity and describes the variation of resistivity with temperature.

Setting the electrical potential at one terminal of the coil heater to the value V_0, which is calculated from the material resistivity and the induced current, and the other terminal to zero volts or ground resulted in resistive loss that occurs in the heater coil structure. The resistance of the heater coil depends on its length l, cross sectional area A, and electrical resistivity ρ_R. So the generated electrical power P in the heater coil is calculated as follows:

$$P = V_0 . I = R . I^2 = \frac{1}{A} . \rho_R . I^2 \quad (4)$$

The joule heating equation (5) is the main equation for governing the time - dependent heat distribution through all the solid parts of the sensor, including the coil element, the metallic structure and the plastic housing:

$$\rho Cp(\partial T/\partial t) - \Delta(k.\Delta T) = Q \quad (5)$$

With the following material properties ρ is the density, C_p is the heat capacity, k is the thermal conductivity, Q is the heat source. The change of temperature in time t depends on the total power dissipation density Q:

$$Q = {}^{P}/_{V} \quad (6)$$

Where, V is the volume of the heater element. In contrast to the generated energy in the coil heater, the heat dissipates via the surface of the heater is described by a Robin boundary condition:

$$k\,(\partial T/\partial n) = \alpha(T)(T_{amb} - T) \quad \text{on } \partial\Omega_{ext} \tag{7}$$

Where $\partial T/\partial n$ represents the normal derivative of T, $\partial\Omega_{ext}$ the exterior boundary of the heater, T_{amb} represents the ambient temperature, α (T) is the heat transfer coefficient, which is temperature dependent and has a significant influence on the solution of the system. It is represented by lower, upper, and vertical surface heat transfer coefficients, α_l, α_u and α_v respectively. In general, it is mainly consisting from two components, radiation α_r and convection α_c:

$$\alpha = \alpha_r + \alpha_c \tag{8}$$

The radiation part of the heat transfer coefficients is calculated by Stefan- Boltzmann law. The rate of heat transfers between the hot surface and its surroundings by radiation Q_{rad} is dependent on the emissivity ε, Stefan- Boltzmann constant σ_s = 5.67e-8 $W/m^2 \cdot K^4$, and on the ambient temperature:

$$Q_{rad} = \varepsilon\sigma_s(T^4{}_{amb} - T^4) = \alpha\,(T_{amb} - T) \tag{9}$$

Since the heater coil is covered by a thin layer of ceramics (alumina in our model) and the cavity between the coil and the ceramics is too small, so the dominant heat transfer is surface to surface radiation or conduction if there are any contact points. Also, as initial condition, the temperature of the solid materials is set to the ambient temperature T_{amb} and the electrical potential to zero. On the other hand, the heat transfer from hot surfaces of the sensor to ambient air by natural convection Q_{conv} can be written as the following:

$$Q_{conv} = A \times h \times (T_{hot\,surface} - T_{amb}) \tag{10}$$

Where, A is area of hot surface and h is convection heat transfer coefficient, which is $5W/m^2.K$ for air. The equations have been solved under Dirichlet, Neumann, and mixed boundary conditions numerically using the Finite Element Method (FEM). When the joule heating module is selected in COMSOL 4.3, fixed temperature and potentials is applied at the terminals of the heater. So, as initial condition the temperature of the solid materials is set to the ambient temperature T_{amb}, and the electrical potential to zero. Several properties of the used materials are required to solve the mathematical equations mentioned above.

The nickel- chrome, platinum, alumina material properties are built in the Comsol software, but for the third material deliverp1 the chemical composition and material properties are listed below in Tables 1,2. Also, properties for semiconductor materials, SnO_2 and ZnO are used as specified in semiconductor hand book.

Element	Ni	Co	Mn	Si	C	Fe
value	29	≤17	≤ 0.35	≤ 0.15	≤ 0.02	Bal

Table 1: Chemical composition (wt%) of Dilverp1 material [28].

Density (g/cm^3)	Resistivity (Ω.m)	Thermal conductivity (W/m.˚C)	Specific heat (J/kg.˚C)	CTE in (1/˚C)	Yield strength (MPa)	Tensile strength (MPa)	Poisson's ratio	Melting point(˚C)
8.25	$49x10^{-8}$	17.5	500	$4\text{-}5.2x\ 10^{-6}$	680	700	0.3	1450

Table 2: Physical properties of Dilverp1 material [28].

Simulation Analysis

Convection and Radiation

Now, implemented the effects of natural heat losses represented by convection cooling and surface to ambient radiation on the upper surface of the whole structure will result in reducing the surface temperature of the helical coil, from 366 to 178˚C in case of applying convection cooling factors, and to 109˚C in case of applying convection cooling simultaneously with surface radiation effects. While in meander coil, the surface temperature is decreased from 373 to 178˚C with convection cooling and to 108˚C in case of applying convective and radiation effects simultaneously. Also, in case of excluding the coil itself from the natural cooling factor assuming that the heater coil itself is protected by alumina tube, and applying 0.15A or 30mW power consumption at the coil terminals, a surface temperature rises to 349˚C for helical coil, and to 356˚C for meander shaped coil. Also, uniform heat distribution was achieved, as shown in Figure 3. These results showed that the meander coil has higher surface temperature than the helical coil under the same conditions.

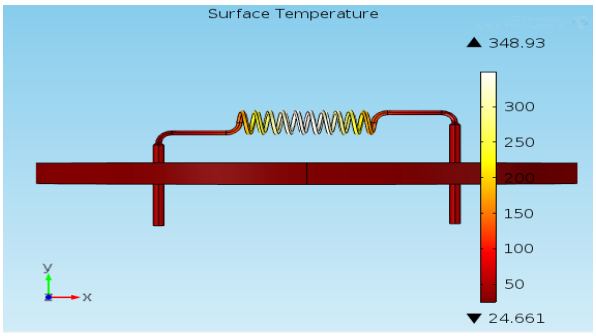

(a)

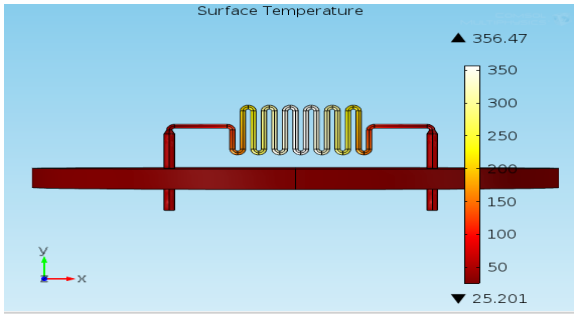

(b)

Figure 3: Effects of natural convection and radiation on the surface temperature of the heater coils, with excluding the heater coil itself from the natural cooling factors **(a)** helical coil **(b)** meander coil.

Ambient Temperature Variations

The variation in ambient air temperatures also contributes a temporal instability for gas sensor parameters [30,31]. As it is well known, ambient temperature during the year can change widely. Such as in Northern Europe ambient temperature during the year can change from −30˚C to +30˚C. Using constant power source (0.15A), the variation in ambient temperature changes the sensor surface temperature, as well as the sensing performance. Also, the natural cooling factors are directly related to the ambient temperature (see related formulas 8-10). Both heater coils were tested by varying the ambient temperature from 0-50˚C, which covers the most operating temperatures for such environmental gas detection sensors. The main characteristics are represented by the maximum and minimum surface temperatures of the heater coil, which will indicate the thermal distribution through the coil structure. The simulation results are listed in Table 3. Notice that the relation between the surface temperatures is linear, as shown in Figure 4. Also, the difference between the maximum and minimum surface temperature is not affected by the variation of ambient temperature. In addition to that, helical coil has better thermal distribution than a meander shaped coil.

T_{amb} (ambient temperature in ˚C)	Helical heater coil		Meander shaped heater coil	
	Coil temperature ˚C Minimum-maximum	Temperature distribution(T_{max}-T_{min})	Coil temperature ˚C Minimum-maximum	Temperature distribution(T_{max}-T_{min})
0	95.09 – 330.35	235.26	92.24-337.85	245.61
5	99.74 – 334.99	235.25	96.89-342.51	245.62
10	104.39 – 339.64	235.25	101.55-347.16	245.61
15	109.03– 344.29	235.25	106.21-351.81	245.6
20	113.68 – 348.93	235.25	110.86-356.47	245.61
25	118.32 – 353.58	235.26	115.52-361.13	245.61
30	122.97 – 358.23	235.26	120.18-365.78	245.6
35	127.61 –362.88	235.27	124.84-370.44	245.6
40	132.26 – 367.53	235.27	129.50-375.10	245.6
45	136.91 – 372.18	235.27	134.16 - 379.76	245.6
50	141.56 – 376.83	235.27	138.83-384.42	245.59

Table 3: Ambient temperature with thermal distribution and maximum temperature achieved through both helical and meander coils, using the FEM simulation by Comsol 4.3.

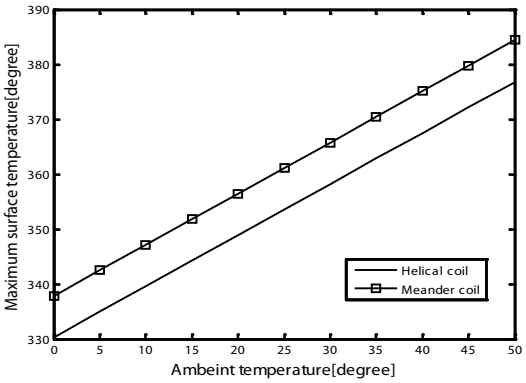

Figure 4: Maximum surface temperature in (˚C) with ambient temperature for both helical and meander coil, without convection and radiation effects on the heater coil itself.

Varying Dimensions

Minimizing the dimensions of different parts in the sensor can significantly reduce the thermal losses due to the convection and radiation. So, minimizing the radius of plastic board (FR4) from 10mm to 8mm will increase the maximum surface temperature from 349 to 377˚C for helical coil, and from 356 to 367˚C for meander coil. In contrast, increasing the radius of copper- nickel pins connected to the heater terminals from 200µm to 500µm will decrease the maximum surface temperature from 377 to 370˚C for helical coil, and from 367 to 359˚C for the meander coil. The coil dimensions also are simulated. For the helical coil, the simulation results of using nickel - chrome coil with different dimensions are shown in Table 4.

Table 4: Simulation results for different diameter and length for nickel-chrome helical coil.

Maximum surface temperature (˚C)	Number of turns	Outer diameter of the heater coil (µm)	Internal diameter of the heater coil (µm)
279.11	10	500	100
358.53	10	550	150
411.02	10	600	200
445.88	10	650	250
469.54	10	700	300
238.1	15	700	300
148.02	20	700	300

Varying Heater Coil Materials

Also, testing different materials to achieve good thermal distribution, maximum surface temperature from 350-360˚C, and low power consumption is also simulated using nickel – chrome alloy, platinum, and Delvirep1 materials. Also, the transient response was investigated. We confirmed that among these materials, platinum has the best response time and thermal distribution, but the most power consumption of 105 mW. And since the surface area is not directly connected to the sensitive layer, the thermal distribution will be investigated on the sensitive layer later on. So, the most appropriate material for the heater among them was nickel - chrome alloy material, for its low power consumption, as shown in Tables 5,6.

Heater coil material	Helical heater coil		Meander shaped heater coil	
	Heater coil temperature ˚C) (minimum-maximum)	Thermal distribution ($T_{max.}$ - $T_{min.}$)	Heater coil temperature ˚C) (minimum-maximum)	Thermal distribution ($T_{max.}$ - $T_{min.}$)
Ni-Cr alloy	113.68 – 348.93	235.25	110.86-356.47	245.61
pt	25.44 – 30.59	4.83	24.96-30.34	5.38
Delvirp1	59.50 – 151.93	84.2	58.32-154.01	95.69

Table 5: Different materials for both heater coil with their related surface temperatures and thermal distribution using 0.15 A.

Heater coil material	Helical heater coil			Meander shaped heater coil		
	Power consumption (mW)	Heater coil temperature (˚C) Minimum- maximum	Thermal distribution ($T_{max.}$ - $T_{min.}$)	Power consumption (mW)	Heater coil temperature (˚C) Minimum- maximum	Thermal distribution ($T_{max.}$ - $T_{min.}$)
Ni-Cr alloy	30	113.68 – 348.93	235	30	110.86-356.47	246
Pt	105	203.89 – 353.91	150	105	176.66- 353.54	177
Delvirp1	35	141.82 – 355.58	214	35	115.08-356.60	242

Table 6: Different materials of heater coil with their related power consumption to achieve maximum surface temperature between 350-360˚C.

Implementation of Alumina Material and Sensitive Layer

Semiconductor sensor has a thermally conductive layer (Alumina) surrounded the heater coil and transfer the heat to the sensitive layer such as tin dioxide SnO_2 layer deposited on its surface, it has also two electrodes made of gold. These electrodes detect the change in resistance when a target gas reacts with the sensing layer of metal oxide. For a gas sensor to operate at maximum performance the temperature distribution on the sensing layer must be uniform. This uniform distribution is achieved and the maximum temperature of the sensing layer is at the centre of the coil length where most of the adsorption takes place. Therefore, the power consumption depends upon the geometry and type of material used for heating purpose.

Using alumina as the electrically insulated layer on both coils as a solid structure with 200µm thickness beyond the coil boundaries, and applied current of 0.65A resulted in maximum surface Temperature of 469˚C for the helical coil with 629mW power consumption and 412˚C for the meander coil with 643mW power consumption. This result confirmed that the helical coil generates higher surface temperature with lower power consumption. Also, both coils have approximately same thermal distribution through the surface of an alumina structure (with a maximum temperature difference of 8˚C for each coil) as shown in Figure 5. Knowing that, the meander heater coil is widely used in MEMS technology nowadays for its easier fabrication processes, and mechanical stability comparing with the helical coil.

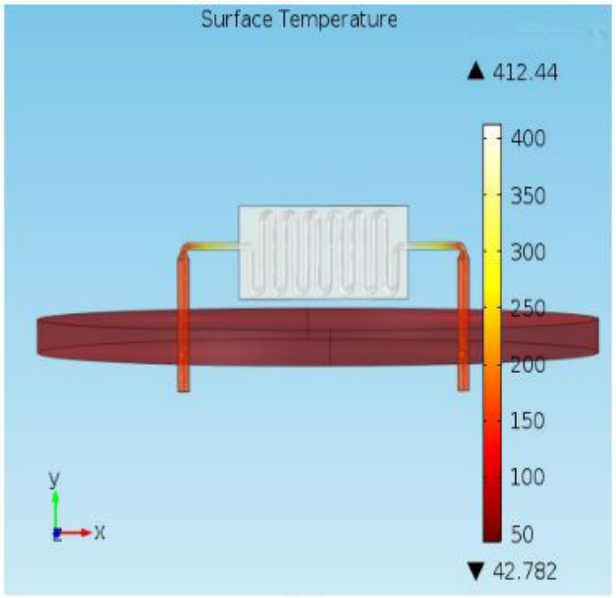

(a)

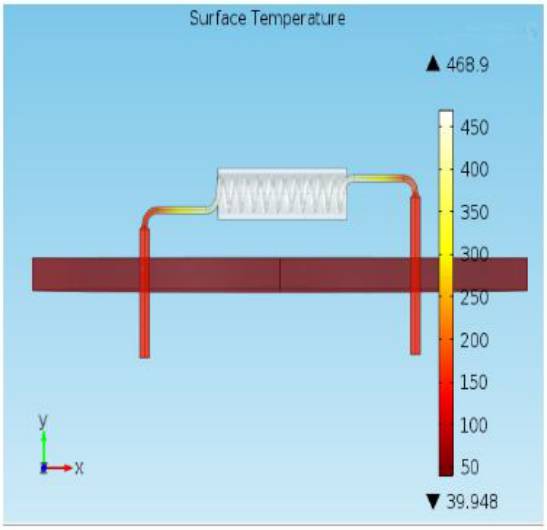

(b)

Figure 5: Surface temperature of Alumina material (a) helical coil (b) meander shaped coil.

Results and Discussions

The helical heater coil is usually used in porous tube semiconductor gas sensors and the meander shaped coil is extensively used in thin and thick film gas sensors [119]. So these two coil structures are simulated. Firstly, nickel-chrome alloys material was used for helical coil, with internal radius of 100µm, outer radius of 500µm, and 10 turns. A plastic board of 10mm radius and FR4 material is implemented. While the meander coil wire radius is 100µm. The simulation is carried out by applying current source of 0.15A initially. After that, a block of Alumina material, and 100µm thickness for sensitive layer were simulated. The temperature of the heater coil was analysed, considering the convection and radiation losses. The simulation results showed that the meandering coil is more affected than the helical one by 31% at 30mW power supply. Also, varying ambient temperatures were simulated using supply voltage of 1V. As a result, changing T_{amb} in the range of 0-50˚C didn't affect the thermal distribution, but increase the surface temperatures in linear relation for both coils. This is shown in Figure 6.

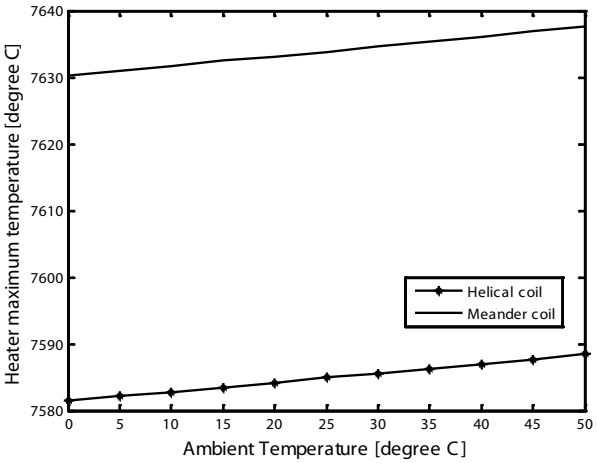

Figure 6: Maximum surface temperature for both helical and mender coil versus ambient temperature, and supply voltage of 1V.

On the other hand, the lateral dimensions of the sensor structure have a significant role on the maximum surface temperature. For both designs, minimizing the diameter of plastic board will reduce the heat losses, due to convection and radiation, so raising the surface temperature. Also, increasing the diameter of nickel-copper plated pins will reduce the surface temperature, due to increasing the surface of the pins. So, the heat losses will be increased. Now, the coil dimensions represented by wire diameter and the total coil length are related directly to the resistance value of the coil. As shown in formula (4) above, ρ_R is the electrical resistivity and depends on the material of the wire, l is the length of the coil, and A is the cross sectional area of the wire. Thus, the diameter of the wire is inversely proportional to the resistance of the coil and proportional to the surface temperature. In contrast, the length of the wire is directly proportional to the resistance of the coil so inversely proportional to the surface temperature.

In addition, different materials for heater coils are investigated, and the results showed that the platinum has better thermal distribution, while the nickel-chrome required the minimum power consumption among the tested materials for both heater coils. This is due to the thermal properties of these materials. The power consumption calculated based on the supply voltage and resistance of each material as observed in Figures 7, 8. As a result shown below, Ni-Cr material needs minimum power consumption as 18% of the Pt power consumption (1.12W) to achieve 2200-2600˚C, and moderate response time (Figure 9). Dilverp1 has the maximum response time, as shown in Table 7.

Heater material	Supply voltage - V	Resistance - Ohm	Power consumption - W	Time response (t_{90}) - seconds
Ni-Cr	0.5	1.25	0.2	37.5
Pt	0.4	0.143	1.12	11
Dilverp1	0.45	0.6	0.338	67

Table 7: Power consumption for helical heater coil using different materials.

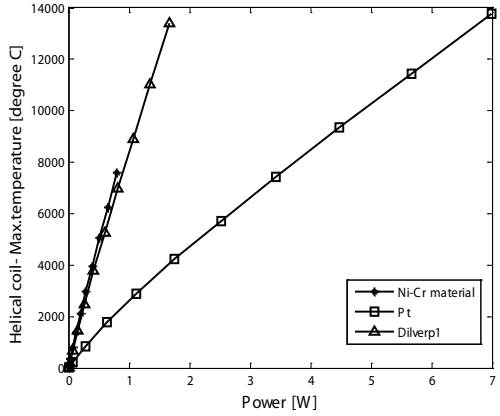

Figure 7: Maximum surface temperature for helical coil using different materials and power supplies.

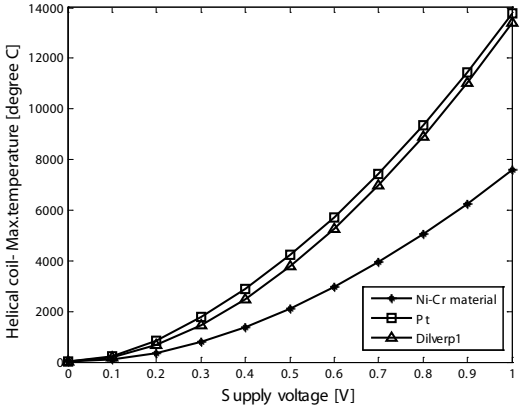

Figure 8: Maximum surface temperature for helical heater coil using different material.

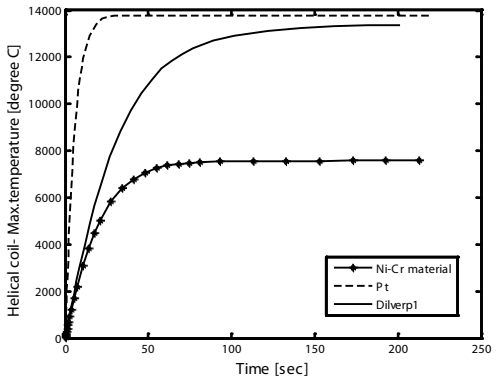

Figure 9: Time response for surface temperature of helical heater coil.

Furthermore, adding alumina material resulted in minimizing the surface temperature. So, using 0.65A in simulation showed that the helical coil generates a surface temperature higher than the meander one, with lower power consumption. This is due to the heat that concentrates at the core of the helical coil. So, alumina material can transport the heat effectively, due to its high thermal conductivity. Also, applying natural cooling effects such as convection and surface radiation resulted in heat losses. The meander coil losses the heat more than the helical coil by 31% at 30mW. Finally, two different materials were simulated for the sensitive layer of hydrogen sensor, SnO_2 and ZnO material. The time dependent analysis (transient analysis), shows the time required to reach 90% of the maximum temperature for both materials. As a result, shown in Figure 10, it's clear that both sensitive materials will achieve the same surface temperature in each design and using the same power. But, for helical design, both of sensitive material will achieve higher surface temperature by 36% from the meander based design sensor at 500mW power supply.

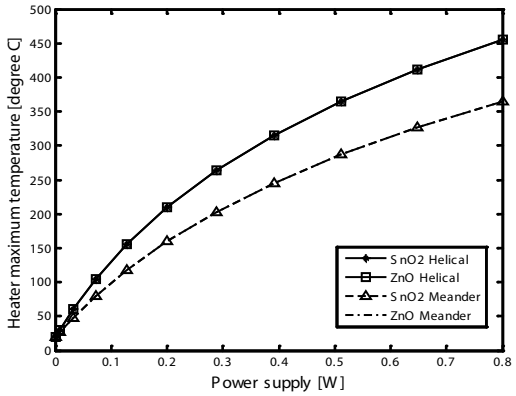

Figure 10: Maximum surface temperatures of sensitive materials with different power supply for helical and meander coils.

Moreover, the time response (related to surface maximum temperature) for both sensitive materials is not the same. SnO_2 response time (t_{90}, which need to achieve 90% of the maximum temperature) is faster. The response time of SnO_2 material- sensor is faster by 28% and 31% of ZnO response for helical and meander based sensor respectively, see Figure 11. More details are observed in Table 8.

Sensitive layer materials	Heater design	Time response (t_{90}) - seconds
SnO_2	Helical coil	36.5
SnO_2	Meander coil	50
ZnO	Helical coil	51
ZnO	Meander coil	72

Table 8: Time response for SnO_2 and ZnO materials using helical and meander based sensors.

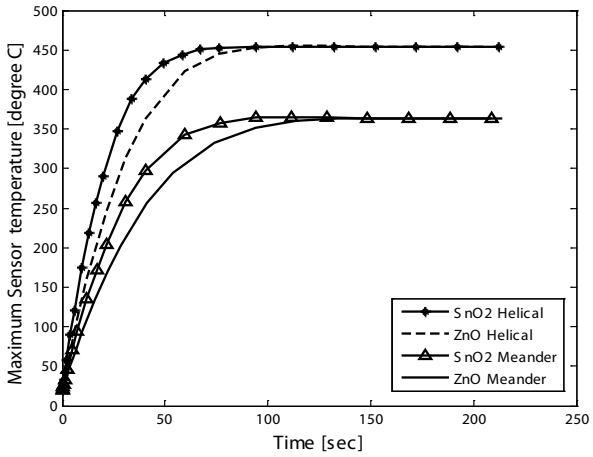

Figure 11: Time response of heating process for the MOS sensor, using different sensitive materials with both heater design, helical and meander coil.

Also, the sensor surface temperature not significantly affects by changing the ambient temperature from 0-50˚C. The change in both sensor design temperatures not exceeds 8˚C, as observed in Figure 12.

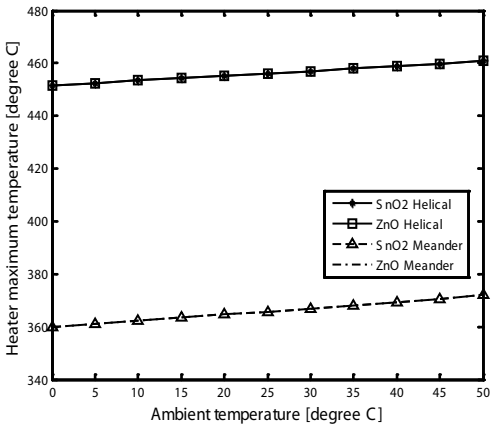

Figure 12: Sensor surface temperature with ambient temperature (0-50˚C).

Finally, as well known, MOS gas sensors suffer from high operating temperature (300-500˚C) and high power consumption. For example, Taguchi gas sensors require 230-760 mW [32]. In this study, the commercially sensor scale and dimensions were approximately simulated to investigate some parameters. As a result, the simulated sensors need 400-500 mW to generate 350-400˚C. In literature, there is no simulation study investigate the whole sensor structure (MOS), by means of thermal or transient analysis. Mostly, the heater device was the main investigated element in the sensor. So, to compare the results of this study with literature, some of literature simulation results related to micro-heater thermal analysis using FEM is mentioned in Table 9.

Study	Heater material	Power consumption-mW	Response time (thermal response)-seconds	Ref.
Micro-heater simulation; 350-450˚C.	Pt- different geometries	20-40	-	Bansal V et al. [33]
Micro-heater simulation; 472˚C	- Pt	- 182	Rising time: 0.7e-3	Sinha S et al. [32]
	-Poly silicon	- 189		
	-Dilverp1	- 145		
Micro-heater simulation; 450-480˚C.	-Pt	- 43.1	-	Monika et al. [34]
	-Poly silicon	- 28.3	-	
	-Dilverp1	- 18.5	-	
This study: 1.Micro-heater 350-360˚C.	-Ni-Cr	-30	- 37.5	
	- Dilverp1	- 35	- 11	
	- Pt	- 105	- 67	
2. Whole sensor structure; 350-360˚C.	- Ni-Cr; Helical based sensor	-400	SnO_2: 36.5	
			ZnO : 51	
	- Ni-Cr; Meander based sensor	-600	SnO_2: 50	
			ZnO: 72	

Table 9: Some of literature simulated results related to micro-heater thermal analysis (used for gas sensor applications).

Conclusions

This simulation and modelling work concluded the following results:

- Comparing two heater designs, the meander coil is affected by natural cooling factors more than the helical one. Its losses the heat more than the helical by 31% at 30mW power supply.
- Changing the ambient temperature directly affects the heat losses caused by convection and radiation linearly. So, changing the ambient temperature from 0-50˚C in both sensor designs resulted in small variation in the surface temperature for both sensor designs, but not more than 8˚C.
- Changing the lateral dimensions of the sensor and the dimensions of the heater coil itself resulted in changing the achieved surface temperature as well as the power consumption. So, the study confirmed that minimizing the size of the sensor will significantly reduce the power consumption.

- Investigating different materials for heater coil, shows that the nickel-chrome material needs minimum power consumption of 82% lower than Pt power consumption. But it has longer response time, which is 37 seconds (240% of Pt response time) at 1V power supply.
- Comparing SnO_2 and ZnO sensitive material for both sensor designs, SnO_2 material has a response time lower than ZnO material by 28% in helical based sensor and 31% in meander one.
- The helical based sensor needs power less than meander one by 40% to achieve the 350°C surface temperature. In other words, the helical based sensor generates higher surface temperature by 36% from the meander one at 500mW power supply.

References

1. Seiyama T, Kato A, Fujiishi K, Nagatani M (1962) A new detector for gaseous components using semiconductive thin films. Anal Chem 34: 1502-1503.
2. Kolmakov A, Moskovits M (2004) Chemical sensing and catalyst by one-dimensional metal oxide nanostructures. Annual Review of Materials Research 34: 151-180.
3. Comini E, Bratto C, Faglia G, Ferroni M, Vomiero A, et al. (2009) Quasi-one dimensional metal oxide semiconductors: preparation and characterization and application as chemical sensors. Progress in Materials Science 54: 1-67.
4. Comini E, Faglia G, Sberveglieri G, Pan Z, Wang Z (2002) Stable and highly sensitive gas sensors based on semiconducting oxide nanobelts. Applied Physics Letters 81: 1869-1871.
5. Kolmakov A, Zhang Y, Cheng G, Moskovits M (2003) Detection of CO and O_2 using tin oxide nanowire sensors. Advanced Materials 15: 997-1000.
6. Wan Q, Li Q, Chen Y, Wang T, He X, et al. (2004) Fabrication and ethanol sensing characteristics of ZnO nanowire gas sensors. Applied Physics Letters 84: 3654-3656.
7. Jing Z, Zhan J (2008) Fabrication and gas-sensing properties of porous ZnO nanoplates. Advanced Materials 20: 4547-4551.
8. Kim I, Rothschild A, Lee B, Kim D, Jo S, et al. (2006) Ultrasensitive chemiresistors based on electrospun TiO_2 nanofibers. Nano Letters 6: 2009-2013.
9. Devi G, Hyodo T, Shimizu Y, Egashira M (2002) Synthesis of mesoporous TiO_2-based powders and their gas-sensing properties. Sensor Actuators B 87: 122-129.
10. Moon H, Shim Y, Kim D, Jeong H, Jeong M, et al. (2012) Self-activated ultrahigh chemo-sensitivity of oxide thin film nanostructures for transparent sensors. Scientific Reports 2: 588.
11. Li X, Lou T, Sun X, Li Y (2004) Highly sensitive WO_3 hollow-sphere gas sensors. Inorganic Chemistry 43: 5442-5449.
12. Zhang D, Liu Z, Li C, Tang T, Liu X, et al. (2004) Detection of NO_2 down to ppb levels using individual and multiple In_2O_3 nanowire devices. Nano Letters 4: 1919-1924.
13. Li C, Zhang D, Liu X, Han S, Tang T, et al. (2003) In_2O_3 nanowires as chemical sensors. Applied Physics Letters 82: 1613-1615.
14. Kim H, Choi K, Pan A, Kim I, Kim H, et al. (2011) Template-free solvo thermal synthesis of hollow hematite spheres and their applications in gas sensors and Li-ion batteries. Journal of Materials Chemistry 21: 6549-6555.
15. Chen J, Xu L, Li W, Gou X (2005) Fe_2O_3 nanotubes in gas sensor and lithium-ion battery applications. Advanced Materials 17: 582-586.
16. Gopel W, Schierbaum K (1995) SnO_2 sensors: Current status and future trends. Sensors and Actuators B 26: 1-12.
17. Korotcenkov G (2007) Metal oxides for solid-state gas sensors: what determines our choice? Mater Sci Eng B 139: 1-23.
18. Shukla S, Zhang P, Cho J, Ludwig L, Seal S (2008) Significance of electrode spacing in hydrogen detection for tin oxide-based MEMS sensor. Int J Hydrogen Energy 33: 470-475.
19. Matbouly H, Domingue F, Palmisano V, Boon-Brett L, Post MB, et al. (2014) Assessment of commercial micro-machined hydrogen sensors performance metrics for safety sensing applications. international journal of hydrogen energy 39: 4664-4673.
20. Dibbern U (1990) A substrate for thin film gas sensors in microelectronic technology. Sensors and Actuators B 2: 63-70.
21. Briand D, Krauss A, van der Schoot B, Weimar U, Barsan N, et al. (2000) Design and fabrication of high-temperature micro-hotplates for drop-coated gas sensors. Sensors and Actuators B 68: 223-233.
22. Sujatha L, Selvakumar V, Aravind S, Padamapriya R, Preethi B (2012) Design and analysis of micro-heaters using COMSOL multiphysics for MEMS based gas sensor. Proceedings COMSOL conference 2012.
23. Graf M, barrettino D, kristein K, hierlemann A (2006) CMOS microhotplate sensor system for operating temperatures up to 500˚C. Sensors and Actuators B 117: 346-352.
24. Gotz A, Gracia I, Cane C, Lora-Tamayo E (1997) Thermal and mechanical aspects for designing micro-machined low power gas sensors. J Micromech Microeng 7: 247-249.
25. Heiling A, Barsan N, Weimar U, Schweizer-Berverich M, Gardner J, et al. (1997) Gas identification by modulating temperatures of SnO_2-based thick film sensors. Sensors Actuators B 43: 45-51.
26. Cavicchi R, Suehle J, Kreider K, Gaitan M, Chaparal P (1996) Optimized temperature-pulse sequences for the enhancement of chemically specific response patterns from micro-hotplate gas sensors. Sensors Actuators B 33: 142-146.
27. Sung J, Lee Y, Lim J, Hong Y, Lee D (2000) Sensing characteristics of tin dioxide/gold sensor prepared by coprecipitation method. Sens Actuators B 66: 149-152.
28. Wisitsoraat A, Tuantranont A, Lomas T (2006) Design and simulation of electro-fabricated MEMS micro-hotplate for gas sensor applications. International MEMS Conference.
29. Bijoy K, Pallavi K, Saral S, Subir K (2011) Design and electro-thermal analysis of MEMS based micro-hotplate for gas sensor. Chennai and Dr. MGR University Second International Conference on Sustainable Energy and Intelligent System.
30. Gong J, Chen Q, Lian M, Liu N, Daust C (2006) Temperature feedback

control for improving the stability of a Semiconductor-Metal-Oxide (SMO) gas sensor. IEEE Sensor J 6: 139-145.

31. Hossein-Babaei F, Ghafarinia V (2010) Compensation for the drift-like terms caused by environmental fluctuations in the responses of chemoresistive gas sensors. Sensors and Actuators B 143: 641-648.

32. Sinha S, Roy S, Sarkar C (2011) Design & Electro-thermal analysis of microheater for low temperature MEMS based Gas Sensor.International Symposium on Devices MEMS, Intelligent Systems & Communication (ISDMISC) 2011 Proceedings published by International Journal of Computer Applications (IJCA): 26-31.

33. Vineet B, Anil G, Dinesh K, Prasad B (2011) 3-D Design Electro-Thermal Simulation and Geometrical Optimization of Spiral Platinum Micro-heaters for Low Power Gas Sensing Applications Using COMSOL. Proceedings COMSOL conference.

34. Monika, Arora A (2013) Design and Simulation of MEMS based Microhotplate as Gas Sensor. International Journal of Advanced Research in Computer Engineering & Technology (IJARCET) 2: 2487-2490.